Determining Maximum MPP-Tracking Sampling Frequency for Input-Voltage-Controlled PV-Interfacing Converter

Jyri Kivimäki*, Moshe Sitbon**, Sergei Kolesnik**, Alon Kuperman** and Teuvo Suntio*

*Department of Electrical Engineering, Tampere University of Technology, Finland

**Department of Electrical Engineering, Ariel University, Israel

Abstract—A maximum-power-point tracking (MPPT) algorithm is essential in all controllers of solar power electronic converters due to the nonlinear current-voltage characteristics of a photovoltaic generator. One of the most widely utilized algorithms are perturbative MPPT techniques such as perturb and observe and incremental conductance methods due to their simple implementation with relatively good tracking performance. However, in order to optimize the performance of such algorithms, the design parameters – sampling frequency and perturbation step size – need to be designed in respect to interfaced power electronic converter. Recent studies have provided state-of-art MPP-tracking design rules for single and two-stage grid-connected PV systems. Unfortunately, the analysis of those studies does not provide analytical results for PV power transient response under feedback-controlled converters. This paper provides reduced-order transfer functions for the converters equipped with either I-type or PID-type controllers in order to approximate the maximum sampling or perturbation frequency for MPP-tracking algorithms. The analysis reveals the factors affecting the transient behavior similarly as in open-loop converter providing valuable tools for optimizing MPP-tracking perturbation frequency design.

I. INTRODUCTION

A maximum-power-point tracking algorithm is essential in all controllers of solar power electronic converters due to the nonlinear current-voltage characteristics of a photovoltaic generator (PVG). One of the most widely utilized algorithms are perturbative maximum-power-point (MPP) tracking techniques such as perturb and observe (P&O) and incremental conductance (IC) methods due to their simple implementation with relatively good tracking performance. These algorithms can be designed either to maximize the energy yield or, with a few modifications, limit the active power in order to prevent exceeding certain power level in the power grid [1], [2]. In both cases, however, the parameters of a tracking algorithm need to be optimized to obtain the highest tracking accuracy. The problem in optimization process of the fixed-step perturbative algorithms is the well-known trade-off between fast tracking performance and low steady-state oscillations, which requires more detailed analysis of the PV system to tune the algorithm design parameters: perturbation step-size and sampling frequency or perturbation frequency. Furthermore, it has been shown that those algorithms can be confused, and operation point can drift further from an MPP if the design parameters are not properly chosen [3].

The perturbation frequency of MPP-tracking process is recommended to be designed by assuming that the operating point lies at the MPP in [3], where PV dynamic resistance is known to equal the corresponding static resistance [4]. It is well known that PV dynamic resistance ($r_{\rm pv}$) affects the dynamic behavior of the PV-interfacing converter [5], [6], [7]. Its main effect is usually the modification of the damping behavior of the internal resonance of the duty-ratio-operated or open-loop converter [5]. According to Fig. 1, we can conclude that the damping of converter resonant behavior would be minimized, when the operating point is moved into the constant-current region (CCR) due to the high value of the dynamic resistance. In case of a duty-ratio-operated MPP-tracking converter, this also means that the PV-power-transient-settling time will be longest in CCR, and thus the maximum perturbation frequency shall be determined by assuming the operating point to lie in CCR as well [8]. The basic principle to select the proper perturbation step size is to ensure that the power change induced by the perturbation step shall always be higher than the power change induced by the change in the environmental conditions during the perturbation interval [3]. In practice, the maximum PV power change caused by the changes in the environmental conditions will take place when the operating point lies at the MPP [3].

Similar perturbation-frequency design rules are not available or published for input-voltage-feedback-controlled PV-interfacing converters: Ref. [9] recommends to using simulation to extract the proper settling time, which can be then used to compute the maximum allowed perturbation frequency according to the guidelines presented in [3]. Ref. [10] recommends to using perturbation frequency less than 1/10 of the input-voltage-feedback-loop crossover frequency without any scientific arguments. This paper will provide the missing information by first proving that in case of a input-voltage-feedback-controlled PV-interfacing converter under direct-duty-ratio (DDR) control, the PV-power-settling time will not be any more dependent on the properties of the PV generator, but only on the design of the input-voltage feedback loop. In case of cascaded control (i.e., current-mode control), the dependency on the PV-generator properties may exist and therefore, the methods presented in this paper may not be valid [11], [12]. This paper will further show that the dynamic behavior of the PV-power transient can be character-

ized by means of the undamped natural frequency (ω_n) and damping factor (ζ) of the closed-loop system. The simulated and experimental evidence is provided using a boost-power-stage converter [7], which validates the proposed methods to be sufficiently accurate with certain limitations.

II. GENERAL DYNAMICS OF PV POWER

A simplified electrical equivalent circuit of a PV cell composes of a photocurrent source with a parallel-connected diode and parasitic elements, where photo-induced current is linearly depended on the irradiance level, and the series and parallel resistances represent various nonidealities in a real PV cell. The relation between diode current and voltage can be modeled with an exponential equation, yielding a nonlinear resistance that can be used to analyze the PV effect on switched-mode converter dynamics [13]. From the power electronics point of view, the behavior of the dynamic (r_{pv}) and static ($R_{pv} = V_{pv}/I_{pv}$) resistances of the solar cell are very important because the dynamic changes in the power electronic interfacing converters are dependent on the ratio of the dynamic and static resistances.

The I-V curve of a PV generator (cf. Fig. 1) contains basically two distinct regions separated by the MPP (i.e., CCR) at the voltages less than the MPP voltage, and constant-voltage (CVR) region at the voltages higher the MPP voltage, which are categorized based on the variable, which stays practically constant within the named region. The finite resolution of the digitally controlled measurement system will make it impossible to locate exactly the MPP and therefore, the vicinity of MPP will form a region, which can be named as constant-power region (CPR) (cf. Fig. 1). The existence of the CPR is actually utilized in the MPP-tracking algorithm known as ripple correlation control [14]. The low-frequency dynamic resistance (r_{pv}) of the PV generator follows the similar resistance behavior characteristic to the named electrical sources as well [6]. At the MPP, the static (R_{pv}) and dynamic (r_{pv}) resistances are equal [4]. In the other regions, the static resistance (R_{pv}) (i.e., V_{pv}/I_{pv}) behaves as shown in Fig. 1. The normalization in Fig. 1 is done by dividing i_{pv} and v_{pv} by their MPP values (i.e., 0.91 A & 16.0 V), r_{pv} is divided by its maximum value (i.e., 1 kΩ) as well as R_{pv} by the maximum value of r_{pv}, respectively.

The dynamics related to PV power can be approximated as follows

$$\hat{p}_{pv} = V_{pv}\hat{i}_{pv} + I_{pv}\hat{v}_{pv} + \hat{v}_{pv}\hat{i}_{pv}, \qquad (1)$$

which can be derived from the definition of power in terms of voltage and current (i.e. $p_{pv} = (V_{pv} + \hat{v}_{pv})(I_{pv} + \hat{i}_{pv})$) and discarding the steady-state value at the operation point. If considering only the dynamic behavior of the PV power induced by a step-change at the operation point of the DC-DC converter (i.e. irradiance and output voltage variations of DC-DC converter are neglected) then (1) can be given by

$$\hat{p}_{pv} \approx V_{pv}\left(\frac{1}{R_{pv}} - \frac{1}{r_{pv}}\right)\hat{v}_{pv} - \frac{\hat{v}_{pv}^2}{r_{pv}}, \qquad (2)$$
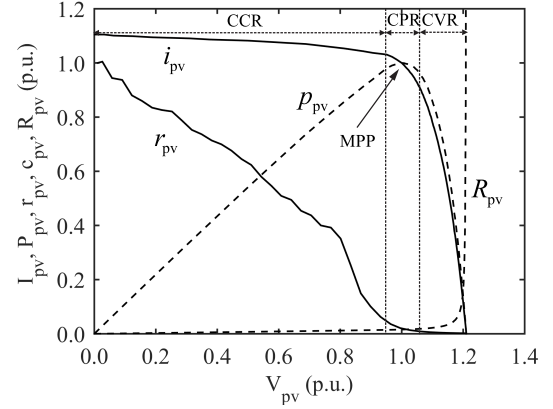

Fig. 1. Normalized behavior of I_{pv}, P_{pv}, r_{pv}, and R_{pv} as function V_{pv} when the operating point is varied.

because $\hat{i}_{pv} \approx -(1/r_{pv})\hat{v}_{pv}$ and static PV resistance equals $R_{pv} = U_{pv}/I_{pv}$. According to (2), we can state that the PV power ripple can be defined in CCR by $\hat{p}_{pv} \approx I_{pv}\hat{v}_{pv}$ (i.e., $r_{pv} \gg R_{pv}$), in CPR by $\hat{p}_{pv} \approx -\hat{v}_{pv}^2/R_{pv}$ (i.e., $r_{pv} = R_{pv}$), and in CVR by $\hat{p}_{pv} \approx (-V_{pv}/r_{pv})\hat{v}_{pv}$ (i.e., $R_{pv} \gg r_{pv}$), respectively, based on the behavior of r_{pv} and R_{pv} at the different operation points of the PV generator in Fig. 1. Therefore, the behavior of the PV power transient can be predicted by studying the dynamic resistance r_{pv} and perturbed PV voltage $\hat{v}_{pv}$ in different operational regions [8].

III. PV-INTERFACING CONVERTER OPERATING AT CLOSED LOOP

Figure 2 illustrates a grid-connected two-stage PV system, where PV interface can be disturbed by the change in irradiation (i.e., direct effect on the photovoltaic current i_{ph}), the settling behavior of the DC-DC converter, and the ripple of the DC-link voltage caused, for example, by the grid power fluctuation at twice the grid frequency, etc. In order to capture the effect of these noise sources on the behavior of the PV power (p_{pv}), voltage (v_{pv}), and current (i_{pv}), the dynamic constellation of the PV-generator-converter interface can be given as shown in Fig. 3, where all the vital elements are considered. The notation $\hat{c}$ in Fig. 3 denotes the duty ratio ($\hat{d}$) when the DC-DC converter is applied at open loop and the PV-voltage reference ($\hat{v}_{ref-pv}$) when the DC-DC converter is applied at closed loop, respectively. In principle, all the information given below is equally valid for a single-stage PV system, but the analysis of such a system may be more challenging due to the complexity of the inverter. It shall also be understood that the controlled-source elements (i.e., G_{ci} and T_{oi}) can be affected by the load impedance or the inverter input impedance, which can naturally change the dynamic behavior of the DC-DC converter.

A. PV-Interfacing Converter Operating at Open Loop

The MPP-tracking converters can be operated at open loop, i.e., the perturbation is applied directly to the duty ratio of the corresponding converter or at closed loop, where the feedback
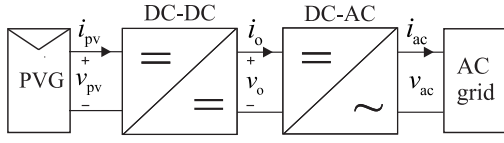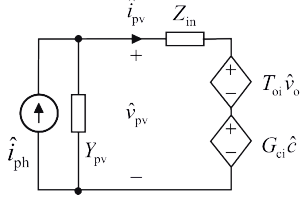
Fig. 2. A grid-connected two-stage PV system.

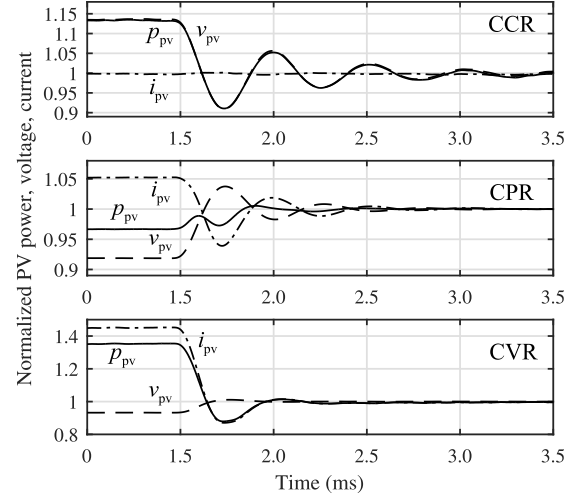Fig. 3. The dynamic representation of the PV-generator-converter interface.

Fig. 4. Behavior of PV voltage (dashed line), current (dash-dotted line), and power (solid line) when a step change in a duty ratio is applied in a duty-ratio-operated boost-power-stage converter in different PV-generator operational regions. [8]

variable is the PV voltage and the perturbation is applied to the reference of PV voltage [6]. The controlled variable cannot actually be the PV current because of the current-source nature of the PV generator, which would cause a violation of Kirchhoff's current law and saturation of the controller especially during the varying climatic conditions as discussed and demonstrated explicitly in [6]. The MPP-tracking design variables are the size of perturbation step and the sampling frequency of the PV voltage and current, which is usually also the same as the perturbation frequency. If the size of the perturbation step is too small and/or the sampling frequency is too high, then the MPP-tracking process can become unstable because the computed voltage derivative of the PV power does not comply to the real derivative [3], [9], [15]. The reasons for the errors can be the change of irradiance level, the ripple in the measured variables or the transient settling process of the corresponding power electronic converters [15].

According to Fig. 3, we can compute that the dynamic related to the PV voltage and current can be given by [13]

$$
\begin{aligned}
\hat{v}_{pv} &= \frac{Z_{in}}{1 + Z_{in}Y_{pv}}\hat{i}_{ph} + \frac{T_{oi}}{1 + Z_{in}Y_{pv}}\hat{v}_o + \frac{G_{ci}}{1 + Z_{in}Y_{pv}}\hat{c} \\
\hat{i}_{pv} &= \frac{1}{1 + Z_{in}Y_{pv}}\hat{i}_{ph} - \frac{Y_{pv}T_{oi}}{1 + Z_{in}Y_{pv}}\hat{v}_o - \frac{Y_{pv}G_{ci}}{1 + Z_{in}Y_{pv}}\hat{c},
\end{aligned}
\tag{3}
$$

where $\hat{c}$ denotes the general control variable (i.e., in this case, the perturbed PV-voltage reference), G_{ci}, T_{oi} and Z_{in} denote the control-to-input-voltage transfer function, output-to-input or reverse transfer function, and input impedance of the PV interfacing converter, respectively. It is well known that the temperature of the PV modules has significant effect on the PV power but its dynamics is quite slow due to the large thermal capacity of the PV panels as discussed also in [3]. Therefore, its effect is not considered in (3). From the perturbation-frequency design point of view, the control-to-input-voltage-related dynamics is of interest in (3) (i.e., the last terms of the equations in (3)).

The experimental transient waveforms of PV voltage, current, and power shown in Fig. 4 clearly confirms the validity

of the theoretical formulation for the behavior of the PV-power transient in the different operational region. Fig. 4 is constructed in such a manner that all the original waveforms are divided by their final values to maximize the information of the settling behavior: In CCR, the PV-power transient follows the settling behavior of the PV voltage directly. In CPR, the PV-power transient is very small because the PV-voltage and current behaviors tend to cancel each other. In CVR, the PV-power transient follows the settling behavior of the PV current directly. The PV-power settling time is also longest in CCR, which is clearly visible in Fig. 4. The changes in the settling time are induced by the changes in the damping behavior of the internal resonance due to the PV-generator dynamic resistance, which affects the time constant of the system, i.e., $\tau = 1/\zeta_{pv}\omega_n$. The PV-generator-affected damping factor ζ_{pv} of a duty-ratio or voltage-mode-controlled (DDR/VMC) converter can be given in general [7] by

$$
\zeta_{pv} \approx \frac{1}{2}\left(r_{loss}\sqrt{\frac{C_2}{L_1}} + \frac{1}{r_{pv}}\sqrt{\frac{L_1}{C_2}}\right),
\tag{4}
$$

where r_{loss} denotes the parasitic losses of the power-stage components as well as L and C denote the power stage inductance and capacitance values, respectively. The observed settling-time differences in Fig. 4 can be explicitly addressed to the behavior of the time constant according to (4) and the behavior of r_{pv} in Fig. 1.

B. PV-Interfacing Converter Operating at Closed Loop

In case of input-voltage-feedback-controlled converters, the PV-generator effect on the system damping behavior is quite different, especially, when the input-voltage-feedback-loop crossover frequencies are designed to be sufficiently lower or higher than the resonant frequency. That is because the

closed-loop input impedance ($Z_{\text{in}-\text{c}}$) is rather small especially at the frequencies, where the feedback-loop gain is high (i.e. $Z_{\text{in}-\text{c}}Y_{\text{pv}} \approx Z_{\text{in}-\text{c}}/r_{\text{pv}} \ll 1$). The corresponding predicted frequency responses (i.e. $1/(1 + Z_{\text{in}-\text{c}}Y_{\text{pv}})$) are given in Fig. 5, where the solid, dashed, and dash-dotted lines correspond to the operation in CCR, CPR, and CVR, respectively. The figure indicates that the PV generator affects significantly the damping of the internal resonance (i.e., ζ_{pv}) of the converter in CVR. In contrast, it affects only marginally the magnitude of the loop and the phase margin when the crossover frequency of the input-voltage loop gain is located far enough from resonant frequency. Therefore, the set of equations in (3) becomes

$$\hat{v}_{\text{pv}} \approx Z_{\text{in}-\text{c}}\hat{i}_{\text{ph}} + T_{\text{oi}-\text{c}}\hat{v}_{\text{o}} + G_{\text{ci}-\text{c}}\hat{c}$$
$$\hat{i}_{\text{pv}} \approx \hat{i}_{\text{ph}} - Y_{\text{pv}}T_{\text{oi}-\text{c}}\hat{v}_{\text{o}} - Y_{\text{pv}}G_{\text{ci}-\text{c}}\hat{c}, \tag{5}$$

where subscript extension 'c' denotes the closed-loop transfer functions.
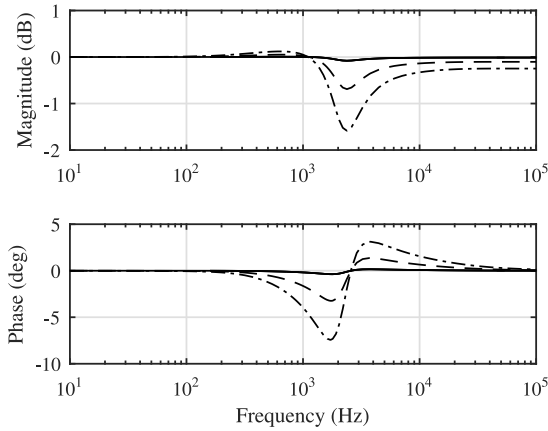

Fig. 5. Predicted PV-generator effect on the closed-loop transfer functions of an input-voltage-feedback-controlled boost power-stage converter (i.e., $1/(1+ Z_{\text{in}-\text{c}}/r_{\text{pv}})$, where the crossover frequency of the input-voltage feedback loop is placed higher than the resonant frequency (i.e., 1 kHz vs. 3 kHz).

If we assume that changes in atmospheric conditions and output voltage $\hat{v}_{\text{o}}$ is negligible, the only relevant elements from the MPP-tracking sampling-frequency point of view are the last right-most elements in (5), where $G_{\text{ci}-\text{c}}$ stands for

$$G_{\text{ci}-\text{c}} = \frac{1}{G_{\text{se}-\text{in}}}\frac{L_{\text{in}}}{1 + L_{\text{in}}}. \tag{6}$$

Therefore, the only stimulus to the PV-generator voltage and current is the voltage reference through the PV-affected loop gain $L_{\text{in}}^{\text{pv}}$ as given by

$$L_{\text{in}}^{\text{pv}} = G_{\text{se}}G_{\text{a}}G_{\text{cc}}G_{\text{ci}-\text{o}}^{\text{pv}}, \tag{7}$$

where G_{se} is the sensing gain, G_{a} is the modulator gain, G_{cc} is the controller transfer function and $G_{\text{ci}-\text{o}}^{\text{pv}}$ refers to the PV-affected open-loop control-to-input voltage transfer function.

Figures 6 and 7 show the frequency responses of the closed-loop control-to-input voltage transfer functions ($G_{\text{ci}-\text{c}}^{\text{pv}}$) by

using I-type controlled (8) and PID-type controlled (9) boost power-stage converter including the effect of PV generator.

$$G_{\text{cc}}^{\text{I}} = \frac{K_{\text{cc}}}{s} \tag{8}$$
$$G_{\text{cc}}^{\text{PID}} = \frac{K_{\text{cc}}(1 + s/\omega_{\text{z1}})(1 + s/\omega_{\text{z2}})}{s(1 + s/\omega_{\text{p1}})(1 + s/\omega_{\text{p2}})}, \tag{9}$$

where $\omega_{\text{z1}}, \omega_{\text{z2}}$ and $\omega_{\text{p1}}, \omega_{\text{p2}}$ equal to zeros and poles of the controller, respectively, It is worth noting that the input-voltage scaling factor ($G_{\text{se}-\text{in}}$) in (6) equals unity in Figs. 6 and 7. According to Fig. 6 , $G_{\text{ci}-\text{c}}$ reassembles a first-order system when the phase margin is rather high (i.e., close to 90 degrees). Correspondingly, Fig. 7 indicates that $G_{\text{ci}-\text{c}}$ resembles a second-order resonant system when the phase margin is in the order of 50 degrees. The next section will introduce methods to find a reduced-order models for the closed-loop converter, which can be utilized in the design of the perturbation frequency in case of closed-loop MPP-tracking converters.
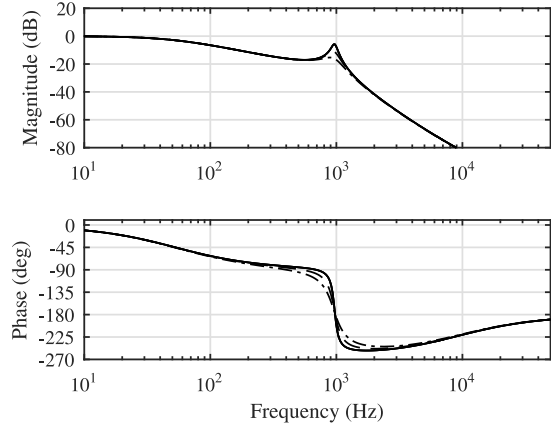

Fig. 6. Estimated frequency response of the closed-loop control-to-input voltage transfer function under I control in different operation regions (CCR: solid line, CPR: dashed line, CVR: dash-dotted line).

IV. MPP-TRACKING PERTURBATION FREQUENCY DESIGN

The behavior of the PV voltage and current transient induced by a step change in the PV reference voltage can be naturally analyzed using software packages as performed, for example, in [3]. This kind of approach does not, however, give enough information on the factors affecting the transient behavior similarly as in case of an open-loop converter in [9]. If the input-voltage loop gain is substituted as such (i.e. (5)) in the corresponding sensitivity function to extract the time-domain functions associated with the corresponding transient behavior, the inverse transformation process will be too complicated and involve unnecessary time functions. Fortunately, settling time of the power transient in closed-loop systems can be approximated by neglecting additional low or high-frequency elements in the input voltage-loop as can be seen from the upcoming analysis.
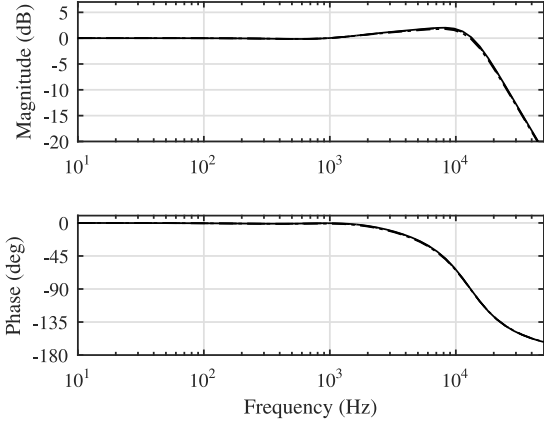
Fig. 7. Estimated frequency response of the closed-loop control-to-input voltage transfer function under PID control in different operation regions (CCR: solid line, CPR: dashed line, CVR: dash-dotted line).

According to Fig. 7, the corresponding closed-loop transfer functions in (6) are clearly of second-order. Therefore, the input-voltage loop gains have to be basically of second-order transfer functions, where the behavior of the transfer functions in the vicinity of the loop crossover frequency will determine the dynamic behavior of the closed-loop system. Correspondingly, the input-voltage loop gains determining the low-frequency behavior can be approximated in case of I control by

$$L_{\mathrm{in-RO}}^{\mathrm{I}} \approx \frac{G_{\mathrm{se}}G_{\mathrm{a}}K_{\mathrm{cc}}V_{\mathrm{e}}}{s}, \tag{10}$$

and in case of PID control by

$$L_{\mathrm{in-RO}}^{\mathrm{PID}} = \frac{G_{\mathrm{se}}G_{\mathrm{a}}K_{\mathrm{cc}}V_{\mathrm{e}}}{\omega_{\mathrm{z1}}\omega_{\mathrm{z2}}} \cdot \frac{\omega_{\mathrm{n}}^2}{s(1+s/\omega_{\mathrm{p2}})}, \tag{11}$$

where $V_{\mathrm{e}} = V_{\mathrm{o}} + V_{\mathrm{D}} + (r_{\mathrm{d}} - r_{\mathrm{ds}})I_{\mathrm{pv}}$. Therefore, the reduced-order closed-loop control-to-input-voltage transfer functions can be given for I control by

$$G_{\mathrm{ci-c}}^{\mathrm{RO-I}} = \frac{1}{G_{\mathrm{se-in}}} \frac{\dfrac{G_{\mathrm{se-in}}G_{\mathrm{a}}K_{\mathrm{cc}}V_{\mathrm{e}}}{s}}{1 + \dfrac{G_{\mathrm{se-in}}G_{\mathrm{a}}K_{\mathrm{cc}}V_{\mathrm{e}}}{s}} \tag{12}$$
$$= \frac{G_{\mathrm{a}}K_{\mathrm{cc}}V_{\mathrm{e}}}{s + G_{\mathrm{se-in}}G_{\mathrm{a}}K_{\mathrm{cc}}V_{\mathrm{e}}}$$

and for PID control by

$$G_{\mathrm{ci-c}}^{\mathrm{RO-PID}} = \frac{\dfrac{G_{\mathrm{a}}K_{\mathrm{cc}}V_{\mathrm{e}}}{\omega_{\mathrm{z1}}\omega_{\mathrm{z2}}} \dfrac{\omega_{\mathrm{n}}^2}{s(1+s/\omega_{\mathrm{p2}})}}{(1+s/\omega_{\mathrm{p2}}) + \dfrac{G_{\mathrm{se}}G_{\mathrm{a}}K_{\mathrm{cc}}V_{\mathrm{e}}}{\omega_{\mathrm{z1}}\omega_{\mathrm{z2}}}} \tag{13}$$
$$= \frac{\dfrac{G_{\mathrm{a}}K_{\mathrm{cc}}V_{\mathrm{e}}\omega_{\mathrm{n}}^2}{\omega_{\mathrm{z1}}\omega_{\mathrm{z2}}}}{s^2 + s\omega_{\mathrm{p2}} + \dfrac{G_{\mathrm{se}}G_{\mathrm{a}}K_{\mathrm{cc}}V_{\mathrm{e}}}{\omega_{\mathrm{z1}}\omega_{\mathrm{z2}}}\omega_{\mathrm{p2}}}.$$

If the roots of the denominator polynomial are well separated, then Eq. (12) can be approximated at low frequencies by

$$\frac{L_{\mathrm{in}}^{\mathrm{I}}}{1 + L_{\mathrm{in}}^{\mathrm{I}}} \approx \frac{\omega_{\mathrm{n}}/2\zeta}{s + (\omega_{\mathrm{n}}/2\zeta)}. \tag{14}$$

Moreover, the equation (13) has similar form as general second-order transfer function, which can be given as follows

$$\frac{L_{\mathrm{in}}^{\mathrm{PID}}}{1 + L_{\mathrm{in}}^{\mathrm{PID}}} \approx \frac{\omega_{\mathrm{n}}^2}{s^2 + s2\zeta\omega_{\mathrm{n}} + \omega_{\mathrm{n}}^2} \tag{15}$$

In case of first-order system (i.e., (14)), the system time constant is $\tau = 2\zeta/\omega_{\mathrm{n}}$, and in case of the resonant type system (i.e., (15)), the system time constant is $\tau = 1/\zeta\omega_{\mathrm{n}}$, respectively. As discussed in case of the open-loop operated MPP-tracking converter, the system time constant will determine the settling time of the power transient as well. According to (12)-(15), the time constants can be given by

$$\begin{aligned} \tau^{\mathrm{I}} &\approx 1/(G_{\mathrm{se-in}}G_{\mathrm{a}}K_{\mathrm{cc}}V_{\mathrm{e}}) \\ \tau^{\mathrm{PID}} &\approx 2/\omega_{\mathrm{p2}}. \end{aligned} \tag{16}$$

In case of resonant system, ω_{n} and ζ can be given based on (13) by

$$\begin{aligned} \omega_{\mathrm{n-RO}}^{\mathrm{PID}} &= \sqrt{\frac{G_{\mathrm{se}}G_{\mathrm{a}}K_{\mathrm{cc}}V_{\mathrm{e}}\omega_{\mathrm{n}}^2}{\omega_{\mathrm{z1}}\omega_{\mathrm{z2}}}\omega_{\mathrm{p2}}} \\ \zeta_{\mathrm{RO}}^{\mathrm{PID}} &= \frac{1}{2}\sqrt{\frac{\omega_{\mathrm{z1}}\omega_{\mathrm{z2}}\omega_{\mathrm{p2}}}{G_{\mathrm{se}}G_{\mathrm{a}}K_{\mathrm{cc}}V_{\mathrm{e}}\omega_{\mathrm{n}}^2}}. \end{aligned} \tag{17}$$

Proper operation of the MPP-tracking process necessitates that the PV power transient has to be settled down to a certain percentage of the final value before the measurement of v_{pv} and i_{pv} can be performed [15]. Based on the prior analysis and computations, the corresponding minimum sampling pace of the MPP-tracking algorithm can be calculated according to the similar principle as done in [3] yielding

$$T_{\mathrm{s}}^{\mathrm{PID}} \approx \frac{2}{\omega_{\mathrm{p2}}} \ln\left(\frac{1}{\Delta\sqrt{1 - \dfrac{\omega_{\mathrm{z1}}\omega_{\mathrm{z2}}\omega_{\mathrm{p2}}}{4G_{\mathrm{se}}G_{\mathrm{a}}K_{\mathrm{cc}}V_{\mathrm{e}}\omega_{\mathrm{n}}^2}}}\right) \tag{18}$$

and in case of first-order system (i.e., (14)) by

$$T_{\mathrm{s}}^{\mathrm{I}} \approx \frac{1}{G_{\mathrm{se-in}}G_{\mathrm{a}}K_{\mathrm{cc}}V_{\mathrm{e}}} \ln\left(\frac{1}{\Delta}\right), \tag{19}$$

which corresponds the time period where the PV power transient has reached $(1 \pm \Delta) \cdot 100$ % of its final steady-state value. The perturbation frequency shall be naturally less than the inverse of the defined settling times in (18) and (19) for ensuring proper operation of the MPP-tracking algorithms [3].

V. REDUCED-ORDER MODEL VERIFICATION

The boost-power-stage converter (cf. Fig. 8) is very often used as the MPP-tracking converter, and therefore, we have taken it also as an example converter in this paper. The information given in the earlier sections is not, however, limited to the boost-type converter but is equally applicable also to the other converters under input-voltage-feedback-operated MPP-tracking mode. More detailed characterization of the PV panel and the dynamic modeling of the boost-power-stage converter in Fig. 8 can be found from [6] and [7], respectively. The operating points, where the transient behavior of the PV power is analyzed, are 0.97 A & 12 V in CCR, 0.91 A & 16 V in CPR, and 0.82 A & 17 V in CVR. The predicted dynamic behavior of the converter is not relevant in the context of the paper but the model given in [7] is shown to be accurate. Fig. 8 shows, in addition to the power stage, also the simplified control system and measurement interface. The output-terminal voltage source is a valve-regulated lead-acid battery of 7.2 Ah with the nominal voltage of 24 V.
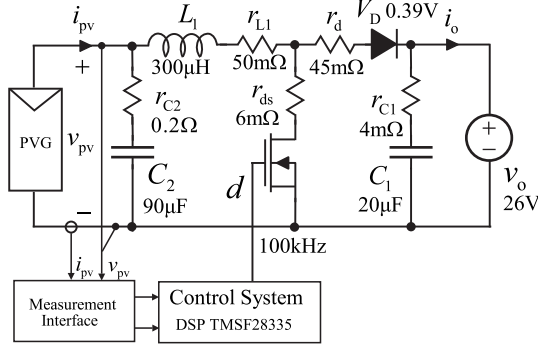
Fig. 8. The schematics of the boost-power-stage converter with component values.

A. Simulated Evidence

Figure 9 shows the estimated frequency responses of input-voltage loop gain (dotted line) vs. the corresponding full-scale frequency responses under the I control. The gain for I-controller is placed at $K_{cc} = 12.6$. Figure 9 indicates that reduced-order method equals original full-order response in the vicinity of the input-voltage-loop crossover frequency (i.e., $\omega_c = 2\pi \cdot 50$ Hz and phase margin (PM) is 89.8 degrees). The corresponding time constant (cf. Eq. (16)) and settling time (cf. Eq. (19)) to the 5-% settling band can be computed to be 3.0 ms and 9.0 ms, respectively. Moreover, Fig. 11 (i.e., the bottom figure) shows the corresponding simulated PV power transient from which the settling time can be found to be approximately 8.3 ms. This shows that the method will give a quite accurate estimate on the settling time when a system has first-order dynamics.

Figure 10 shows the estimated frequency response (dotted line) of input-voltage loop gain vs. the corresponding full-scale frequency responses (solid line) under the PID control. The PID controller parameters in (9) are placed as follows: $\omega_{z1} = \omega_{z2} = 1/\sqrt{L_1 C_2}$, $\omega_{p1} = 1/r_{C2}C_2$, $\omega_{p2} = \pi f_s/3$ and
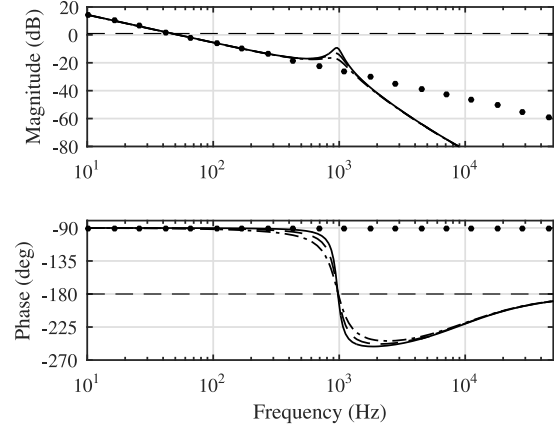
Fig. 9. The reduced-order frequency response (dotted line) vs the full-order frequency response of the input-voltage loop gains under I control in different operation regions (CCR: solid line, CPR: dashed line, CVR: dash-dotted line).

$K_{cc} = 2818$. Figure 10 indicates that the reduced-order model (dotted line) produces a phase response, where the phase margin equals 59 degrees when the original phase margin is 49 degrees. The crossover frequency is at 10 kHz in both cases. According to Eq. (17), the estimated undamped natural frequency (ω_n) and the damping factor (ζ) of the full-order system will be 88.3 krad/s and 0.593, respectively. Therefore, predicted settling time in respect to 5% settling band is 62 μs. Figure 11 (i.e., the top figure) shows the corresponding simulated PV power transient from which the settling time can be found to be approximately 89 μs. As the PM of 59 degrees implies, the reduced-order method gives slightly too short approximation for the settling time. If the resonant frequency had designed slightly lower frequency, reduced-order model would have estimated settling time more accurately.
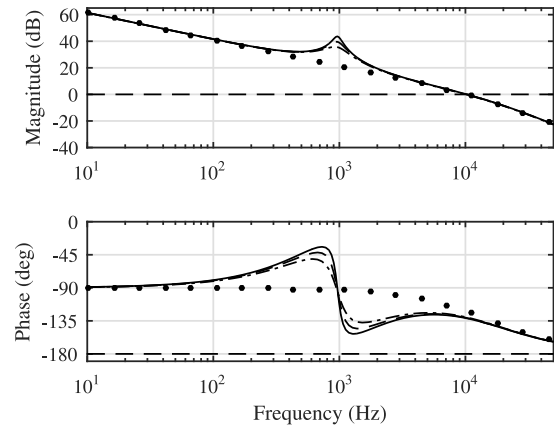
Fig. 10. The reduced-order frequency response (dotted line) vs the full-order frequency responses of the input-voltage loop gains under PID control in different operation regions (CCR: solid line, CPR: dashed line, CVR: dash-dotted line).
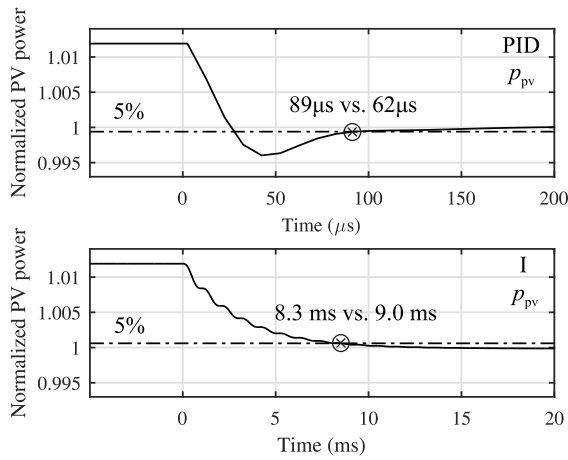
Fig. 11. The simulated power-transient induced by a step change in PV voltage in CCR: (a) under PID control, and (b) under I control.

B. Experimental Evidence

Figure 12 shows the measured PV-generator-affected input-voltage-feedback loop gains in case of I controller, where the effect of PV generator is clearly visible around the internal resonant frequency of the power stage. The crossover frequencies and PMs of converter under I control (Fig. 12) are as follows: : CCR: 54 Hz, 89.6°, CPR: 52.3 Hz, 89.2°, and CVR: 50.5 Hz, 89.0°, respectively. Figure 12 shows that the PV-generator effect on the low-crossover feedback-loop gain is insignificant, and therefore, the crossover frequencies and PMs will stay practically as 50 Hz and 89.0 degrees.
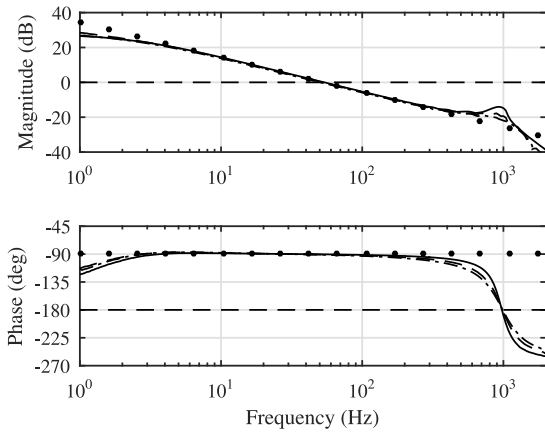

Fig. 12. The measured PV-generator-affected frequency responses of the input-voltage-feedback loops under I control (CCR: solid line, CPR: dashed line, CVR: dash-dotted line and reduced-order model: dotted line).

Figure 13 shows the measured PV-power transient for the I-controlled converter, where the first settling time corresponds to the measured value and the last one to the predicted value. Since the parameters in (19) are the same as in Fig. 11, the time constant and settling time can also be calculated to be 3.0 ms and 9.0 ms, respectively. It can be concluded that the

estimated settling time for I-type control is quite close to the measured settling times in case of 5-% settling band. (Note: The normalization in Fig. 13 is performed by dividing the waveform by its final value.)
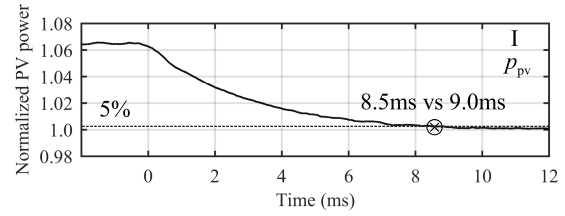

Fig. 13. The measured power-transients induced by a step change in PV voltage in CCR under I control.
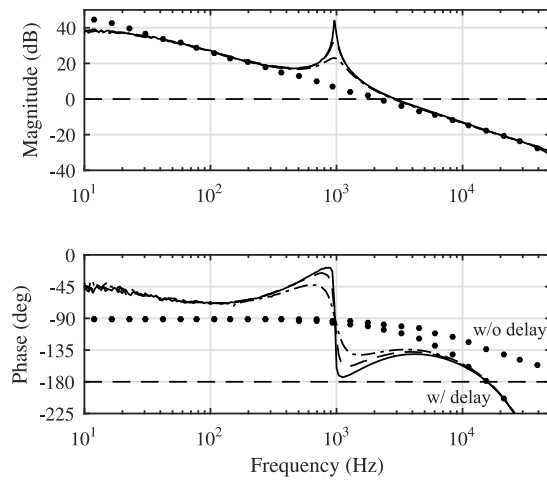

Fig. 14. The measured PV-generator-affected frequency responses of the input-voltage-feedback loops under PID control (CCR: solid line, CPR: dashed line, CVR: dash-dotted line and reduced-order model: dotted line).

Figure 14 shows the measured frequency responses of input-voltage-feedback loops of a boost-power-stage converter, where the PID feedback-loop design have been performed slightly differently what shown in the previous subsections. In this case, the gain K_{cc} for PID controller was selected to be 501 due to existing delay in the system as discussed more detail in the following subsection. Therefore, the crossover frequency of the feedback loop in Fig. 14 is approximately 3 kHz. The corresponding phase behaviors indicate that the phase margin will vary slightly along the changes in the PV-generator operating point (i.e., CCR: 37 degrees, CPR: 41 degrees, and CVR: 45 degrees), which means that the system time constant will also vary accordingly. The variation does not pose problems in perturbation frequency point of view since the model in (13) assumes CCR operation, which will give the longest settling time regardless.

It can be concluded from Fig. 14, however, that in case of PID-type control the resonant frequency is too close to the crossover frequency (i.e., 1 kHz vs 3 kHz) and therefore, the

system cannot be estimated accurately with (15). Moreover, the sampling delay has a significant effect on the phase of the input-voltage loop gain, which can also be noticed by comparing reduced-order transfer functions (dotted lines) in Fig. 14 with and without the effect of delay. The following subsection presents the further discussion about design issues on high-bandwidth controllers.

C. Design Issues

According to Fig. 14, the closed-loop system in (15) will be slightly affected by the PV generator as visible also in Fig. 10. The original crossover-frequency goal was 10 kHz, where the variations in the named parameters would be very small as can be easily detected from Fig. 14. Under digital control, the feedback loop gain will be affected by the sampling delay T_d, which is usually considered to be in the order of $1.5 \times T_{sw}$, where T_{sw} denotes the switching cycle. The delay produces phase shift which would be already close to -45 degrees at 1/10 of the switching frequency posing real problems for control design when the goal is to place the crossover at the corresponding frequencies. As a consequence of this, the crossover frequency was designed to be about 3 kHz. In that case, however, crossover frequency appears to be too close to the resonant frequency and therefore, the second-order model of the closed-loop system does not produce a good approximation of the full-order transfer function in the vicinity of crossover frequency.

In practice, this means that the resonant frequency should be designed to be at lower frequencies so that the crossover would be selected close to 10-times the resonant frequency to reduce more the dependence on the PV generator. Moreover, the switching frequency needs to be about two decades higher than the corresponding crossover frequency in order to achieve sufficient stability margins and approximate system settling time accurately using the second-order model in (15). It is also worth noting that even if there are slight variations in the crossover and PM, they do not affect the closed-loop transient settling time significantly. The most practical case of verifying the designs is to use constant-current input sources, which will yield the worst case in the crossover frequency and PM with respect to the system time constant, i.e., the longest settling time.

VI. CONCLUSION

The paper proposes an analytical method to analyze settling time of PV power transient in input-voltage controlled PV-interfacing converter by focusing on low or high-frequency behavior around the loop gain crossover frequency. Both I-type and PID-type controllers were studied and verified by experimental results. The paper reveals that the closed-loop control-to-input-voltage transfer functions of I-type and PID-type equipped converter can be reduced to first-order and second-order transfer functions, respectively. That enables to approximate PV power transient analytically revealing the factors affecting the transient behavior similarly as in open-loop converter providing valuable tools for determining the

maximum MPP-tracking perturbation frequency. However, it is worth noting that the method has some limitations: The first-order model requires that a resonant frequency needs to be 5-10 times higher than the designed crossover frequency in order to give accurate results. Correspondingly, the second-order model gives a good estimate for a full-order closed-loop system as long as crossover frequency is at least 10 times higher that resonant frequency. In addition, the crossover frequency needs to be about two decades lower than switching frequency in order to prevent phase mismatch due to the sampling delay of a digital control system. Fortunately, it is possible to overcome these limitations and further develop the models by using well-known methods in control engineering.

REFERENCES

[1] A. Ahmed, L. Ran, S. Moon, and J.-H. Park, "A fast pv power tracking control algorithm with reduced power mode," *IEEE Trans. Energy Convers.*, vol. 28, no. 3, pp. 565–575, Sep. 2013.

[2] Y. Yang, H. Wang, F. Blaabjerg, and T. Kerekes, "A hybrid power control concept for pv inverters with reduced thermal loading," *IEEE Trans. Power Electron.*, vol. 29, no. 12, pp. 6271–6275, Dec. 2014.

[3] N. Femia, G. Petrone, G. Spagnuolo, and M. Vitelli, "Optimization of perturb and observe maximum power point tracking method," *IEEE Trans. Power Electron.*, vol. 20, no. 4, pp. 963–973, Jul. 2005.

[4] J. Wyatt and L. Chua, "Nonlinear resistive maximum power theorem, with solar cell application," *IEEE Trans. Circuits Syst.*, vol. 30, no. 11, pp. 824–828, Nov. 1983.

[5] L. Nousiainen, J. Puukko, A. Mäki, T. Messo, J. Huusari, J. Jokipii, J. Viinamäki, D. T. Lobera, S. Valkealahti, and T. Suntio, "Photovoltaic generator as an input source for power electronic converters," *IEEE Trans. Power Electron.*, vol. 28, no. 6, pp. 3028–3038, Jun. 2013.

[6] T. Suntio, J. Leppäaho, J. Huusari, and L. Nousiainen, "Issues on solar-generator interfacing with current-fed mpp-tracking converters," *IEEE Trans. Power Electron.*, vol. 25, no. 9, pp. 2409–2419, Sep. 2010.

[7] J. Viinamäki, A. Kuperman, J. Jokipii, T. Messo, T. Suntio, and M. Sitbon, "Comprehensive dynamic analysis of photovoltaic generator interfacing dc-dc boost power stage," *IET Renew. Power Gener.*, vol. 9, no. 4, pp. 306–314, May. 2015.

[8] J. Kivimäki, A. Kuperman, and T. Suntio, "Sampling frequency design to optimizing mpp-tracking performance for open-loop-operated converters," in *42nd Annu. Conf. IEEE Ind. Electron. Soc. 2016. IECON 2016.* IEEE, 2016. In press.

[9] N. Femia, G. Petrone, G. Spagnuolo, and M. Vitelli, "A technique for improving p&o mppt performances of double-stage grid-connected photovoltaic systems," *IEEE Trans. Ind. Electron.*, vol. 56, no. 11, pp. 4473–4482, Nov. 2009.

[10] R. P. Venturini, V. V. R. Scarpa, G. Spiazzi, and S. Buso, "Analysis of limit cycle oscillations in maximum power point tracking algorithms," *2008 IEEE Power Electron. Spec. Conf.*, pp. 378–384, 2008.

[11] A. Urtasun, P. Sanchis, and L. Marroyo, "Adaptive voltage control of the DC/DC boost stage in PV converters with small input capacitor," *IEEE Trans. Power Electron.*, vol. 28, no. 11, pp. 5038–5048, 2013.

[12] M. Sitbon, S. Schacham, T. Suntio, and A. Kuperman, "Improved adaptive input voltage control of a solar array interfacing current mode controlled boost power stage," *Energy Convers. Manag.*, vol. 98, pp. 369–375, 2015.

[13] L. Nousiainen, J. Puukko, A. Mäki, T. Messo, J. Huusari, J. Jokipii, J. Viinamäki, D. T. Lobera, S. Valkealahti, and T. Suntio, "Photovoltaic generator as an input source for power electronic converters," *IEEE Trans. Power Electron.*, vol. 28, no. 6, pp. 3028–3038, Jun. 2013.

[14] T. Esram, J. Kimball, P. Krein, P. Chapman, and P. Midya, "Dynamic maximum power point tracking of photovoltaic arrays using ripple correlation control," *IEEE Trans. Power Electron.*, vol. 21, no. 5, pp. 1282–1291, Sep. 2006.

[15] N. Femia, G. Petrone, G. Spagnuolo, and M. Vitelli, *Power Electronics and Control Techniques for Maximum Energy Harvesting in Photovoltaic Systems.* CRC Press, 2012.